

## Article

# Degradation of Methylene Blue in the Photo-Fenton-Like Process with WO<sub>3</sub>-Loaded Porous Carbon Nitride Nanosheet Catalyst

Weifan Gao<sup>1</sup>, Guichang Zhang<sup>1</sup>, Xiaoping Zhang<sup>1,2,3,4,\*</sup>, Shaoqi Zhou<sup>1,2,3,4</sup> and Zihao Wang<sup>1</sup>

<sup>1</sup> Guangzhou Higher Education Mega Centre, School of Environment & Energy, South China University of Technology, Guangzhou 510006, China

<sup>2</sup> The Key Laboratory of Pollution Control and Ecosystem Restoration in Industry Clusters of Ministry of Education, Guangzhou 510006, China

<sup>3</sup> Guangdong Provincial Key Laboratory of Solid Wastes Pollution Control and Recycling, Guangzhou 510006, China

<sup>4</sup> Guangdong Provincial Engineering and Technology Research Center for Environmental Risk Prevention and Emergency Disposal, Guangzhou 510006, China

\* Correspondence: xpzhang@scut.edu.cn; Tel.: +86-13678920429

**Abstract:** The catalytic capability of original carbon nitride (CN) is limited by a small specific surface area and high electron–hole recombination rate. In this study, WO<sub>3</sub>-loaded porous carbon nanosheets (MCA-CN/WO<sub>3</sub>) were synthesized by thermal treatment with melamine, cyanuric acid and WCl<sub>6</sub>. The MCA-CN/WO<sub>3</sub> could degrade 98% of the methylene blue (MB) within 30 min in the photo-Fenton-like process, displaying better catalytic activity than the original CN (30%), pure MCA-CN (63%) and original CN/WO<sub>3</sub> (87%). The results of photoluminescence and electrochemical impedance spectroscopy demonstrated that the Z-scheme heterojunction of MCA-CN/WO<sub>3</sub> inhibited the recombination of electrons and holes. In addition, the porous nanosheet structure accelerated the electron transfer and provided abundant active sites for MB degradation. A radical quenching experiment indicated that the Z-scheme heterojunction facilitated the decomposition of H<sub>2</sub>O<sub>2</sub> to produce <sup>1</sup>O<sub>2</sub> for MB degradation. The possible degradation pathways of MB were proposed.

**Keywords:** photo-Fenton-like process; WO<sub>3</sub>-loaded porous carbon nitride nanosheet; Z-scheme heterojunction; MB degradation



**Citation:** Gao, W.; Zhang, G.; Zhang, X.; Zhou, S.; Wang, Z. Degradation of Methylene Blue in the Photo-Fenton-Like Process with WO<sub>3</sub>-Loaded Porous Carbon Nitride Nanosheet Catalyst. *Water* **2022**, *14*, 2569. <https://doi.org/10.3390/w14162569>

Academic Editor: Sergi Garcia-Segura

Received: 24 July 2022

Accepted: 17 August 2022

Published: 20 August 2022

**Publisher's Note:** MDPI stays neutral with regard to jurisdictional claims in published maps and institutional affiliations.



**Copyright:** © 2022 by the authors. Licensee MDPI, Basel, Switzerland. This article is an open access article distributed under the terms and conditions of the Creative Commons Attribution (CC BY) license (<https://creativecommons.org/licenses/by/4.0/>).

## 1. Introduction

Dye wastewater is difficult to deal with due to its characteristics of high chroma and high organic content. Advanced oxidation processes (AOPs) such as photocatalysis, Fenton process, photocatalysis, ozonation, etc., have been extensively used in the actual dye wastewater treatment for their high efficiency, simplicity and no secondary pollution [1,2]. AOPs degrade pollutants into CO<sub>2</sub> and H<sub>2</sub>O by active substances such as hydroxyl radical (•OH), superoxide radical (O<sub>2</sub><sup>•−</sup>), sulfate radical (•SO<sub>4</sub><sup>−</sup>) and singlet oxygen (<sup>1</sup>O<sub>2</sub>). As one of the AOPs, the Fenton process degrades organic pollutants with •OH generated from hydrogen peroxide (H<sub>2</sub>O<sub>2</sub>) activation in the Fe<sup>2+</sup>/Fe<sup>3+</sup> homogeneous system [3]. However, the disadvantages such as narrow pH range, incomplete H<sub>2</sub>O<sub>2</sub> decomposition and formation of numerous iron mud limit the widespread application of the technology [4]. To solve these issues, Fenton-like processes are explored, including fabricating heterogeneous catalysts to substitute for Fe<sup>2+</sup>/Fe<sup>3+</sup>, as well as combining Fenton processes with photocatalysis and electrochemical oxidation. It is found that the photo-Fenton-like process can accelerate the reaction rate and broaden the pH range through the synergy of light and H<sub>2</sub>O<sub>2</sub>. Therefore, it is a promising alternative to the traditional Fenton method.

The key to improving the catalytic rate of photo-Fenton-like processes is to prepare a catalyst with good performance. Carbon nitride (CN) is a conjugated polymer semi-

conductor with a narrow band gap (about 2.7 eV), which has the characteristics of visible light catalytic performance, harmlessness and good stability [5]. Meanwhile, the intrinsic functional groups and vacancies, as well as the  $sp^2$  hybridized configuration of CN, accelerate the generation of electrons [6]. Therefore, CN has developed as a promising material in the Fenton-like process. However, the catalytic capability of original carbon nitride is limited by a small specific surface area and high electron–hole recombination rate [7,8]. Porous carbon nitride nanosheets have a high specific surface area compared to the original bulk carbon nitride, providing more active sites for degradation reactions. In addition, the lamellar structure of CN is beneficial for the electron transfer. Xu et al. synthesized highly porous CN with melamine and cyanuric acid by thermal polycondensation, which exhibited enhanced visible light response and higher electron–hole separation efficiency [9]. Hossein et al. prepared porous CN nanosheets with excellent photodegradation efficiency for Rhodamine B and tetracycline [10]. Based on the above research, fabrication of carbon nanosheets using melamine and cyanuric acid can effectively improve the catalytic performance of CN.

The electron–hole separation efficiency of carbon nitride can be further enhanced by constructing heterojunctions with a metal oxide semiconductor.  $WO_3$  is a nonpoisonous, stable semiconductor photocatalyst with a narrow bandgap (2.7–2.8 eV) and displays high visible light utilization [11].  $WO_3$  exhibits excellent oxidation capacity due to its positive VB edge potential (+3.0 V vs. NHE) [12]. The Z-scheme heterojunction between CN and  $WO_3$  can effectively facilitate the separation of electrons and holes, as well as maintain a high redox capacity [13]. Bai et al. used  $WO_3/g-C_3N_4$  to degrade ciprofloxacin in a photo-electro-Fenton-like system, which revealed enhanced catalytic performance. The results showed that the  $W^{6+}/W^{5+}$  cycle promoted the decomposition of  $H_2O_2$ , and broadened the pH range without iron sludge [14]. Therefore,  $WO_3$  is a good catalyst in photo-Fenton-like processes for the decomposition of  $H_2O_2$  to form an active substance.

In this paper, the modified carbon nitride (MCA-CN) was synthesized by melamine and cyanic acid through thermal treatment. An appropriate amount of  $WO_3$  was loaded on the MCA-CN to synthesize MCA-CN/ $WO_3$  by thermal treatment. The MCA-CN/ $WO_3$  was used to degrade methylene blue (MB) through the photo-Fenton-like process. Compared with original CN, the MCA-CN/ $WO_3$  displayed enlarged specific surface area and accelerated electron–hole separation. As a consequence, the MCA-CN/ $WO_3$  exhibited superior catalytic performance to original CN for MB degradation in a wide pH range. Combined with the free-radical quenching experiment and EPR analysis, the mechanism of the photo-Fenton catalytic processes was proposed. The intermediate products of MB degradation were determined by LC-MS and possible degradation pathways were put forward. The study provides a reference for CN treatment of MB in the photo-Fenton-like process.

## 2. Materials and Methods

### 2.1. Chemicals

All chemicals were reagent grade and used as received. Melamine (ME), cyanuric acid (CA), dimethyl sulfoxide (DMSO), tungsten chloride ( $WCl_6$ ), sodium hydroxide (NaOH), p-benzoquinone (BQ), 5,5-dimethyl-1-pyrroline-N-oxide (DMPO), ethylene diamine tetra acetic acid disodium (EDTA-2Na), L-histidine (L-His), 4-hydroxy-2, 2, 6, 6-tetramethylpiperidine (TEMP) and methylene blue (MB,  $C_{16}H_{20}ClN_3OS$ ) were supplied by Aladdin Ltd. Hydrogen peroxide ( $H_2O_2$ , 30 wt%), isopropyl alcohol (IPA), hydrochloric acid (HCl) and ethanol were obtained from Guangzhou chemical reagent factory. Aqueous solutions were prepared with pure water.

### 2.2. Synthesis of MCA-CN/ $WO_3$

Typically, 5 g melamine and 5.1 g cyanic acid were dissolved in 200 mL and 100 mL DMSO, respectively, and stirred at 25 °C for 20 min to obtain white precipitation. Then, the precipitation was centrifuged, washed and dried at 50 °C for 12 h. The dried white solid

was calcined at 550 °C under a flowing N<sub>2</sub> atmosphere for 4 h [15]. The obtained yellow sample was named MCA-CN.

The MCA-CN/WO<sub>3</sub> catalysts were fabricated by the following steps. Typically, 250 mg MCA-CN and a certain amount of WCl<sub>6</sub> were ground with a small amount of ethanol until the materials turned blue. The blue materials were calcined at a certain temperature in N<sub>2</sub> atmosphere for 1 h to construct a heterojunction (heating rate of 7 °C·min<sup>-1</sup>) [16]. To optimize the WO<sub>3</sub> content, MCA-CN/WO<sub>3</sub> samples with various WO<sub>3</sub> contents (5 wt%, 15 wt%, 25 wt% and 35 wt%) were prepared. Samples 300 °C MCA-CN/WO<sub>3</sub>, 350 °C MCA-CN/WO<sub>3</sub>, 400 °C MCA-CN/WO<sub>3</sub> and 450 °C MCA-CN/WO<sub>3</sub> were obtained when the thermal treatment temperatures were 300 °C, 350 °C, 400 °C and 450 °C, respectively. For comparison, pure WO<sub>3</sub> was synthesized without MCA-CN in the same way, and single MCA-CN was second calcined at 350 °C for 1 h without WCl<sub>6</sub>. The typical synthetic procedure is shown in Figure 1.

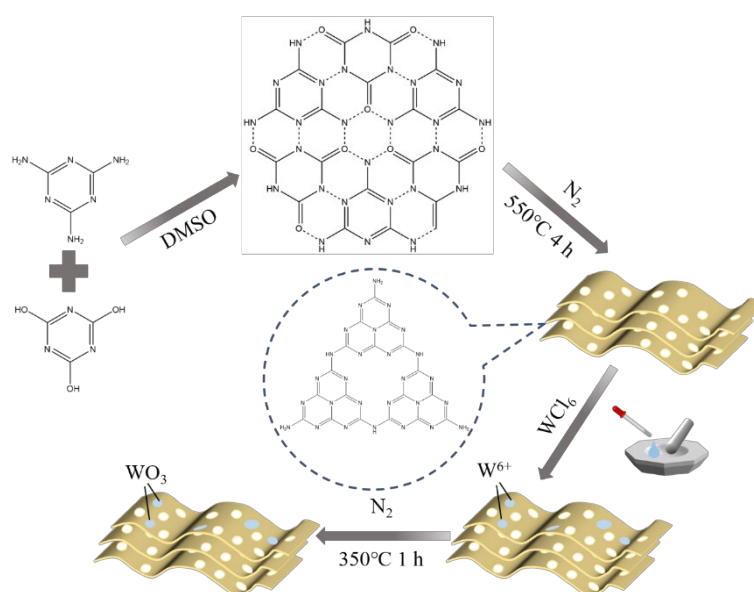


**Figure 1.** The typical synthetic procedure of MCA-CN/WO<sub>3</sub>.

### 2.3. Characterizations

The crystal structure was characterized by X-ray polycrystalline diffraction (XRD, Ultima VI, Akishima-shi, Japan). The geometrical morphology, geometrical size, dispersion state and microelement composition of the material were obtained through scanning electron microscopy (SEM, Merlin Zeiss, Oberkochen, Germany). The morphology, distribution and phase structure of the samples were obtained by 120 kV high-resolution transmission electron microscope (HRTEM, Talos L120c Thermo Fisher, Waltham, MA, USA). Fourier transform infrared spectroscopy (FTIR, infrared thermerfeld IN10, Thermo Fisher Scientific, Waltham, MA, USA) was used to identify the functional groups present in the molecule. The chemical composition and valence band conduction values were obtained by X-ray photoelectron spectroscopy (XPS, Thermo Scientific K-Alpha, Waltham, MA, USA). The pore structure and pore size distribution were characterized by nitrogen adsorption–desorption measurement (Micromeritics APSP 2460, USA). The light absorption range and band gap were obtained by ultraviolet–visible diffuse reflectance absorption spectra (UV DRS, Shimadzu 3600plus, Kyoto, Japan). The charge separation efficiency was detected by photoluminescence spectra (PL, Edinburgh FS5, Livingston, UK) with the excitation wavelength of 380 nm, and <sup>1</sup>O<sub>2</sub> was measured by electron paramagnetic resonance spectrometer (EPR, ELEXSYS-II E500 CW-EPR, Billerica, Germany). The intermediate products of MB degradation were determined by liquid chromatography–tandem mass spectrometry (LC-MS, Ultimate 3000 UHPLC–Q Exactive, Waltham, MA, USA).

#### 2.4. Photocatalytic Test

A typical experimental suspension contained 0.15 g L<sup>-1</sup> MCA-CN/WO<sub>3</sub>, 0.5 mL H<sub>2</sub>O<sub>2</sub> and 20 mg L<sup>-1</sup> MB (100 mL) at pH 7.4 ± 0.1 in a beaker with constant mechanical stirring at 298 ± 2 K. Before analysis, the MB aqueous solution was stirred in darkness for 30 min to achieve adsorption–desorption equilibrium. Next, the degradation reaction was initiated by adding H<sub>2</sub>O<sub>2</sub> and illumination with a 25 W LED lamp (λ > 400 nm). Water samples were taken every five minutes and filtered by a 0.45 μm membrane. The pH value of MB was adjusted by the HCl solution (1 mol L<sup>-1</sup>) and NaOH solution (2 mol L<sup>-1</sup>). The concentration of MB was measured by UV-vis spectrophotometer at the absorption wavelength of 665 nm. The degradation of MB was calculated based on Equation (1) as follows:

$$D = [(C_0 - C)/C_0] \times 100\% \quad (1)$$

where C<sub>0</sub> is the initial concentration of MB at t = 0 and C is the instant concentration at photocatalytic degradation time t (min). Moreover, the kinetics reaction constant (k) is obtained by a pseudo-first-order kinetics model as follows (Equation (2)):

$$\ln(C/C_0) = -kt \quad (2)$$

#### 2.5. Photoelectrochemical Measurement

Photoelectrochemical measurement was carried out on a CHI 660E electrochemical workstation with a three-electrode system. Ag/AgCl electrode and Pt wire were used as reference and counter electrodes, respectively. For the preparation of the working electrode, 10 mg of the sample was mixed with 1 mL ethanol and 80 μL Nafion solution under ultrasonication for 30 min. Then, 40 μL of the suspension was coated on Fluorine-doped Tin Oxide (FTO) glass, and dried at room temperature. Electrochemical impedance spectroscopy (EIS) measurement was measured in a 0.5 M Na<sub>2</sub>SO<sub>4</sub> solution in the frequency range of 0.01 Hz to 100 kHz under the irradiation of 300 W Xe lamps.

#### 2.6. Radical Quenching Experiments

The reactive oxygen species (ROS) including ·OH, h<sup>+</sup>, ·O<sub>2</sub><sup>-</sup> and <sup>1</sup>O<sub>2</sub> were captured by adding a certain amount of isopropyl alcohol (IPA), ethylenediamine tetra acetic acid disodium (EDTA-2Na), p-benzoquinone (BQ) and L-histidine (L-His), respectively. Singlet oxygen (<sup>1</sup>O<sub>2</sub>) was detected in water with 2,2,6,6-tetramethylpiperidine (TEMP) by electron paramagnetic resonance (EPR).

### 3. Results

#### 3.1. Characterization

The SEM images (Figure 2a) showed that the original carbon nitride is lumpy with no obvious pores, while MCA-CN displayed crimped porous carbon nanosheet morphology (Figure 2b). This result indicated that the morphological regulation of carbon nitride by cyanuric acid can make the carbon nitride into loose porous nanosheets, providing more active sites for MB degradation. The lamellar structure ensures strong interaction of carbon nitride and WO<sub>3</sub>, accelerating the electron transfer between carbon nitride and WO<sub>3</sub>. Figure 2c showed the SEM image of MCA-CN/WO<sub>3</sub>, and it can be seen that the structure of MCA-CN was destroyed because of the load of WO<sub>3</sub>. As shown in the TEM images (Figure 2d), MCA-CN/WO<sub>3</sub> exhibited the shape of folded nanosheets. Figure 2e showed the layered structure of MCA-CN/WO<sub>3</sub>, with the lighter region being MCA-CN and the region with the lattice stripe being WO<sub>3</sub>. As shown in the HRTEM image (Figure 2f), the lattice fringes of 0.383 nm corresponded to the (002) crystal plane of WO<sub>3</sub> [14]. The survey spectrum of MCA-CN/WO<sub>3</sub> (Figure 2g) showed the element of carbon and nitrogen accounted for a relatively high proportion. EDX analysis (Figure 2h–k) showed that carbon, nitrogen, oxygen and tungsten elements distributed uniformly in the catalyst, indicating the successful synthesis of MCA-CN/WO<sub>3</sub> [17].

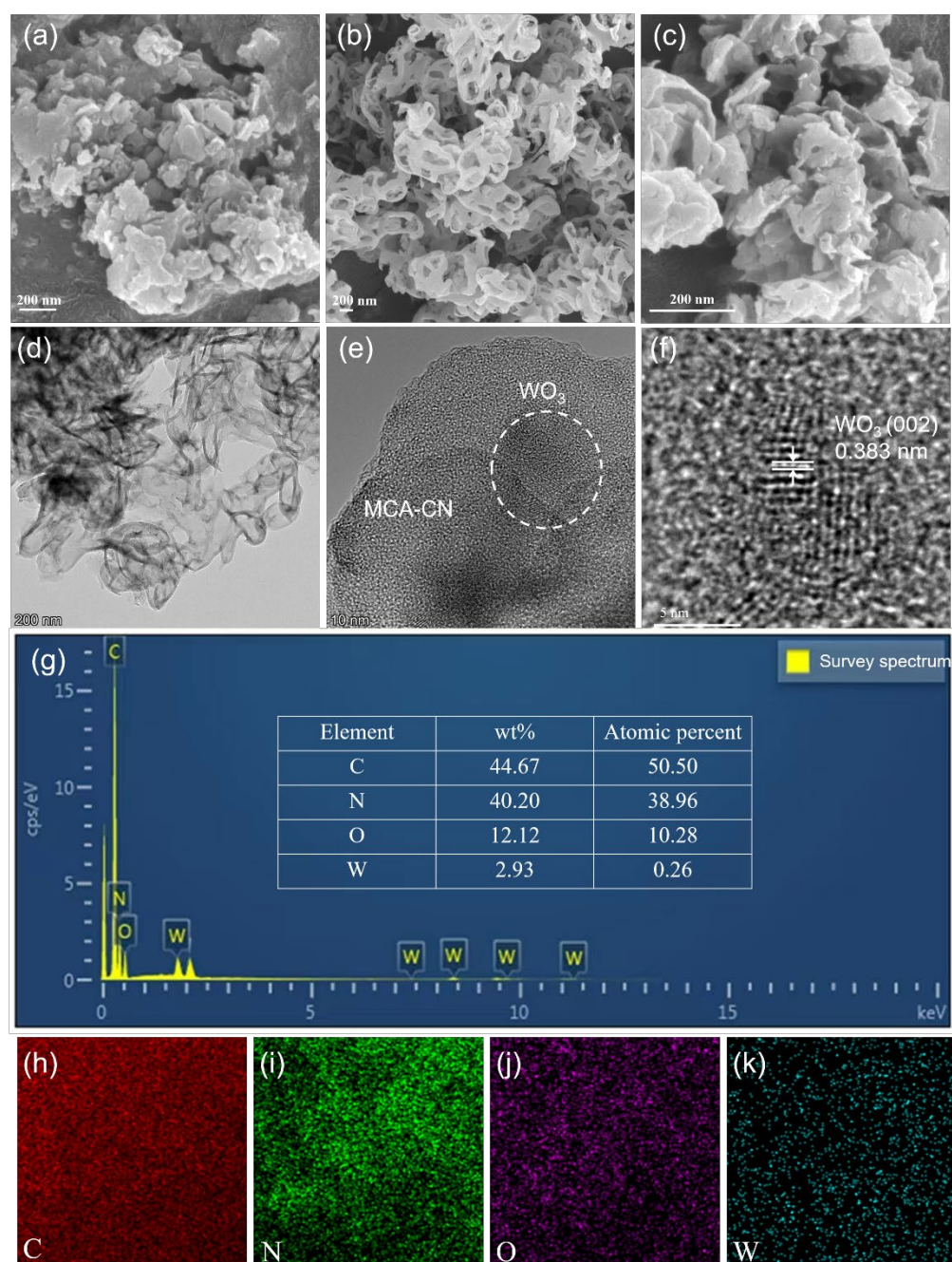


**Figure 2.** SEM images of (a) bulk CN; (b) MCA-CN and (c) MCA-CN/WO<sub>3</sub>. (d–f) TEM images of MCA-CN/WO<sub>3</sub>; (g) survey spectrum of MCA-CN/WO<sub>3</sub> and (h–k) EDX spectrum and elemental mapping images of MCA-CN/WO<sub>3</sub>.

The phase composition of materials was investigated by XRD. As displayed in Figure 3a, MCA-CN showed two characteristic peaks at 27.5° and 12.8°, corresponding to interplanar aromatic stacking (002) and intraplanar stacking (100) of carbon nitride [18]. For MCA-CN/WO<sub>3</sub>, the new diffraction peaks at 23.5° corresponded to the standard card PDF#83-0949 of WO<sub>3</sub>, indicating the successful coupling of WO<sub>3</sub> and MCA-CN. In addition, the broad peak of WO<sub>3</sub> showed amorphous features. Other characteristic diffraction peaks of WO<sub>3</sub> were not observed because of its weak crystallization and low loading content. To further determine the generation of WO<sub>3</sub>, the XRD pattern of pure WO<sub>3</sub> was conducted. Obviously, the diffraction peaks of WO<sub>3</sub> were consistent with the standard card PDF#83-0949, demonstrating the successful generation of WO<sub>3</sub>.

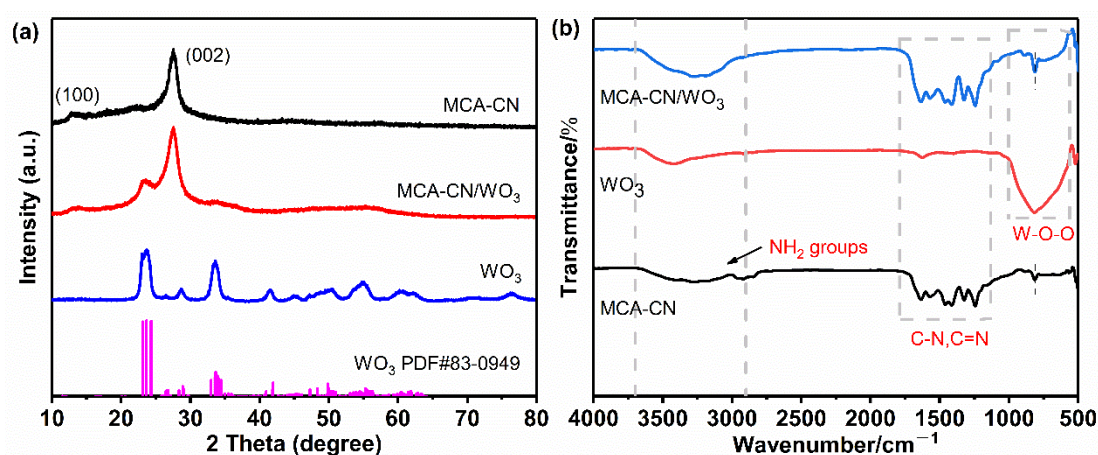


**Figure 3.** (a) XRD patterns of MCA-CN and MCA-CN/WO<sub>3</sub> and (b) FTIR patterns of MCA-CN, WO<sub>3</sub> and MCA-CN/WO<sub>3</sub>.

FT-IR spectra of WO<sub>3</sub>, MCA-CN and MCA-CN/WO<sub>3</sub> are shown in Figure 3b. For pure MCA-CN, the broad absorption vibration peak at 2900–3500 cm<sup>-1</sup> corresponded to the band of N–H or O–H [19]. The absorption band ranging from 1200 to 1600 cm<sup>-1</sup> belonged to the stretch of C–N and C=N in CN heterocycles [20]. The strong absorption vibration peak at 810 cm<sup>-1</sup> was related to the characteristic vibration of the triazine ring unit [21]. For pure WO<sub>3</sub>, the wide absorption peak at 500–1000 cm<sup>-1</sup> corresponded to the vibration of the O–W–O bond [22]. For the MCA-CN/WO<sub>3</sub> composites, the absorption peaks at 1200–1600 cm<sup>-1</sup> were similar to those of MCA-CN, indicating that the structure of MCA-CN was not changed by WO<sub>3</sub>. The typical absorption peak of WO<sub>3</sub> at 500–1000 cm<sup>-1</sup> was also observed in the spectrum of MCA-CN/WO<sub>3</sub>, further proving the successful heterojunction construction of MCA-CN and WO<sub>3</sub> [23].

The elemental composition and surface chemical states of MCA-CN/WO<sub>3</sub> were revealed by XPS. The signals of C, N, O and W elements were observed in the full scan spectrum of MCA-CN/WO<sub>3</sub> (Figure 4a). For the C1s spectrum shown in Figure 4b, the four characteristic peaks at 284.6 eV, 286.5 eV, 288.2 eV and 289.2 eV corresponded to C–C, C–N–C, N–C=N and O–C=O, respectively [24]. The three characteristic peaks of 398.5 eV, 399.5 eV and 401.1 eV in the N1s spectra corresponded to the sp<sup>2</sup> nitrogen N–C=N, N–(C)3 and C–N–H on the triazine ring, respectively (Figure 4c) [25]. As shown in Figure 4d, the O1s spectrum displayed three peaks at 530.6 eV, 532.0 eV and 533.2 eV. The peak at 530.6 eV corresponded to W–O–W in WO<sub>3</sub> [26]. The peak at 532.0 eV was ascribed to the existence of the OH group, which can capture photogenerated holes and inhibit the recombination of electron and hole [27]. The peak at 533.2 eV was related to H<sub>2</sub>O or CO<sub>2</sub> adsorbed from the air. Figure 4e presents the spectrum of W 4f. The peaks at 37.13 eV and 35.07 eV corresponded to W 4f<sub>5/2</sub> and W 4f<sub>7/2</sub> of W<sup>6+</sup>, respectively [11]. Two peaks at 35.8 eV and 33.8 eV were ascribed to W 4f<sub>7/2</sub> and W 4f<sub>5/2</sub> of W<sup>5+</sup> [28].

The N<sub>2</sub> adsorption–desorption isotherms and the Barrett–Joyner–Halenda (BJH) pore size distribution curves of ME-CN, MCA-CN and MCA-CN/WO<sub>3</sub> are displayed in Figure 5. In N<sub>2</sub> adsorption–desorption isotherms, all samples showed type IV isotherms with a type H3 hysteresis loop, indicating the presence of mesoporous structures (Figure 5a). As shown in BJH pore size distribution curves (Figure 5b), all samples exhibited a wide range distribution of pore size. There were two peaks at 2.75 nm and 27.8 nm in the curve of MCA-CN, indicating that the pore size distributed from 2 nm to 30 nm. The BET specific surface area, pore volume and pore size of the materials were calculated by the BJH method and are listed in Table 1. The BET specific surface areas of ME-CN, MCA-CN and MCA-CN/WO<sub>3</sub> composites were calculated to be 10.4, 74.4 and 53.8 m<sup>2</sup> g<sup>-1</sup>. The specific surface area of MCA-CN is 7.1 times higher than that of ME-CN. Obviously, the increased surface area and mesopores of carbon nitride are attributed to the addition of cyanic acid, providing more active sites for catalytic degradation of pollutants. In addition, the porous

structure also contributes to enhanced light absorption, since light is reflected multiple times within the holes. However, MCA-CN/WO<sub>3</sub> had a lower surface area than MCA-CN, because WO<sub>3</sub> is coarse and lumpy with a small specific surface area, and the load of WO<sub>3</sub> covered part of the pores of MCA-CN.

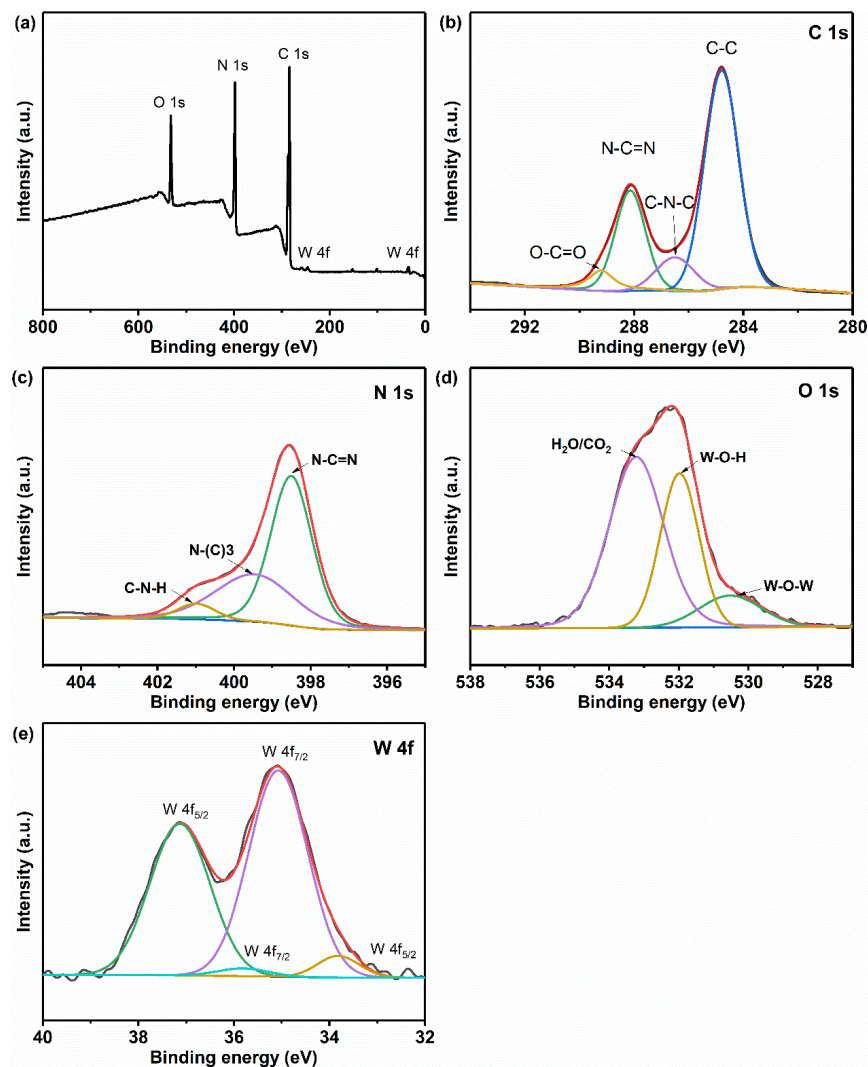


**Figure 4.** XPS spectra of MCA-CN/WO<sub>3</sub>. (a) Survey spectrum. (b) C1s and (c) N1s spectra of MCA-CN/WO<sub>3</sub>. (d) O1s and (e) W 4f spectra of MCA-CN/WO<sub>3</sub>.

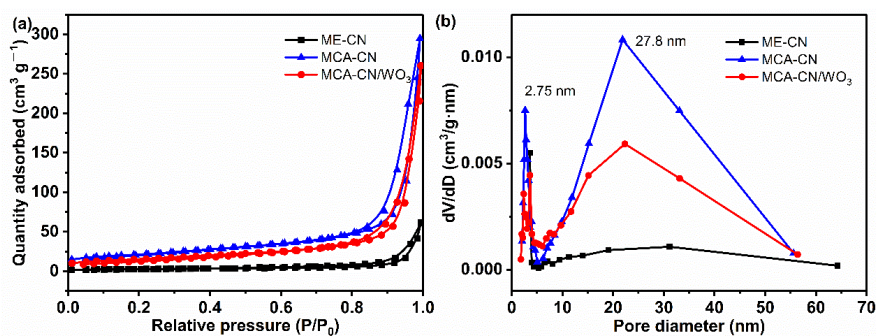


**Figure 5.** (a) N<sub>2</sub> adsorption/desorption isotherm of ME-CN, MCA-CN and MCA-CN/WO<sub>3</sub> and (b) pore size distribution curves of ME-CN, MCA-CN and MCA-CN/WO<sub>3</sub>.

**Table 1.** Surface area, pore volume and pore size of ME-CN, MCA-CN and MCA-CN/WO<sub>3</sub>.

Samples	Surface Area (m <sup>2</sup> g <sup>-1</sup> )	Pore Volume (cm <sup>3</sup> g <sup>-1</sup> )	Pore Size (nm)
ME-CN	10.43	0.025	28.66
MCA-CN	74.44	0.168	24.36
MCA-CN/WO <sub>3</sub>	53.84	0.135	27.50

### 3.2. Photochemical Characterization

The optical performance of the ME-CN, MCA-CN, WO<sub>3</sub> and MCA-CN/WO<sub>3</sub> catalysts were studied by UV-vis DRS. As displayed in Figure 6a, pure MCA-CN exhibited an absorption edge at about 470 nm. Compared with ME-CN (461 nm), the absorption edge of MCA-CN moved to the visible region. This is because the abundant mesopores of MCA-CN can absorb more light radiation. Compared with pure MCA-CN, there was a red shift (490 nm) and significantly enhanced light absorption capacity of MCA-CN/WO<sub>3</sub>, which ascribed to the heterojunction between MCA-CN and WO<sub>3</sub>. Based on the Kubelka–Munk function (Equation (3)), the band gaps ( $E_g$ ) of ME-CN, MCA-CN and MCA-CN/WO<sub>3</sub> were determined to be 2.62, 2.54 eV and 2.41 eV, as depicted in Figure 6b. Figure 6c shows that the  $E_g$  of WO<sub>3</sub> was 2.50 eV. Obviously, the band gap of carbon nitride was effectively reduced by modification of cyanic acid and WO<sub>3</sub>. The reduction in the band gap made it easier for MCA-CN/WO<sub>3</sub> to form photogenerated carriers, promoting the separation of electrons and holes.

$$\alpha h\nu^{(1/n)} = A(h\nu - E_g) \quad (3)$$

where  $\alpha$ ,  $h$ ,  $\nu$  and  $A$  represent the adsorption coefficient, Planck's constant, light frequency and a constant, respectively. The value of  $n$  is determined by the type of semiconductor (1/2 for the indirect band gap and 2 for the direct band gap). Herein, the values of  $n$  for MCA-CN and WO<sub>3</sub> were 2 and 1/2, respectively.

Moreover, the valance band ( $E_{VB}$ ) and conduction band ( $E_{CB}$ ) of MCA-CN and WO<sub>3</sub> could be calculated via the following formulas [29]:

$$E_{VB} = X - E_e + 0.5E_g \quad (4)$$

$$E_{CB} = E_{VB} - E_g \quad (5)$$

where  $X$  is the absolute electronegativity of the catalyst ( $X$ -MCA-CN = 4.72 eV and  $X$ -WO<sub>3</sub> = 6.58 eV) and  $E_e$  is the energy of free electrons vs. hydrogen (4.5 eV). According to the above Equations (4) and (5), the  $E_{VB}$ ,  $E_{CB}$  of ME-CN, MCA-CN and WO<sub>3</sub> are calculated and listed in Table 2. Obviously, there was an alternating band structure between MCA-CN and WO<sub>3</sub>, efficiently improving the photogenerated charge separation and degradation rate of pollutants.

PL spectroscopy under the excitation at 380 nm and EIS spectra were conducted to measure the electron–hole separation rate of MCA-CN/WO<sub>3</sub>. Generally, the weaker the PL intensity, the higher the separation efficiency of catalysts. As shown in Figure 7a, the PL intensity of MCA-CN was weaker than that of ME-CN, implying that MCA-CN exhibited higher electron–hole separation efficiency than ME-CN. Compared with MCA-CN, the significant decrease in PL intensity of MCN indicated the inhibited recombination of electron and hole. EIS spectra are depicted in Figure 7b. The diameter of ME-CN, MCA-CN and MCA-CN/WO<sub>3</sub> decreased in sequence, indicating the lowest electron–hole complexation rate of MCA-CN/WO<sub>3</sub>. Therefore, the nanosheet structure of MCA-CN and the heterojunction between MCA-CN and WO<sub>3</sub> effectively improved the separation efficiency of electron and hole.

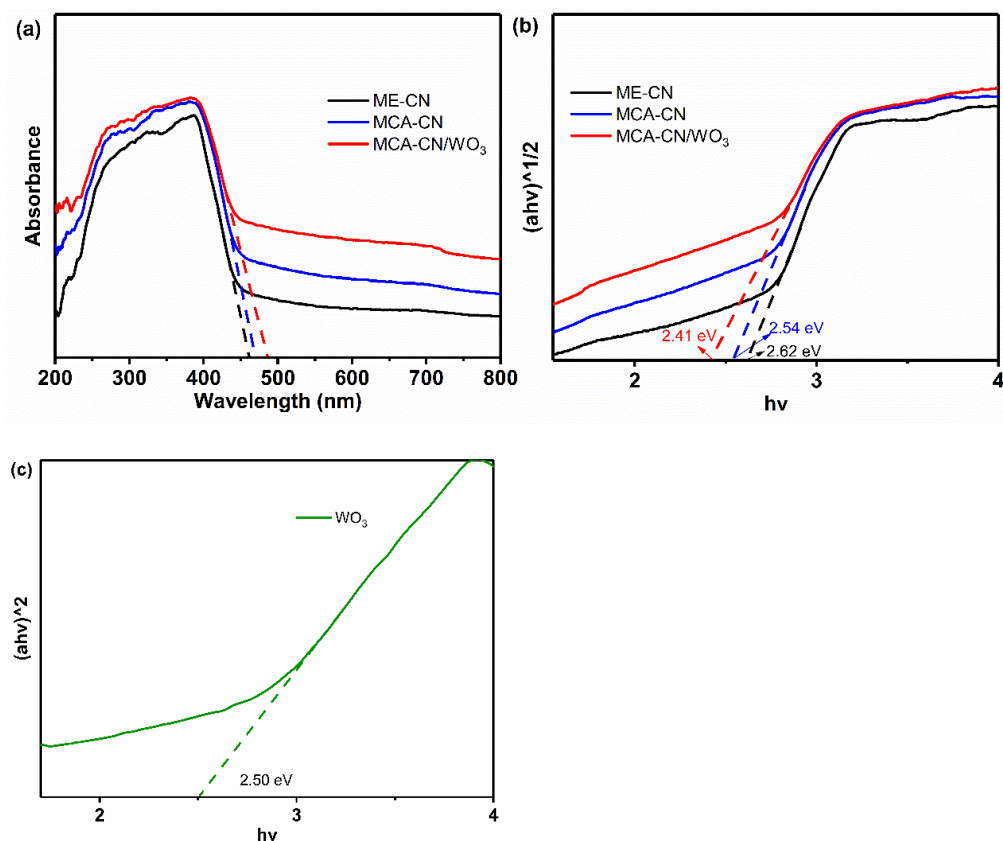


**Figure 6.** (a) DRS of MCA-CN/WO<sub>3</sub>, ME-CN/WO<sub>3</sub> and MCA-CN/WO<sub>3</sub>; (b) corresponding plots of the transformed Kubelka–Munk function; (c) plots of the transformed Kubelka–Munk function.

**Table 2.** Energy Band Potentials of ME-CN, MCA-CN and WO<sub>3</sub>.

Samples	$E_g$ (eV)	$E_{VB}$ (eV)	$E_{CB}$ (eV)
ME-CN	2.62	1.53	−1.09
MCA-CN	2.54	1.49	−1.05
WO <sub>3</sub>	2.50	3.33	0.83

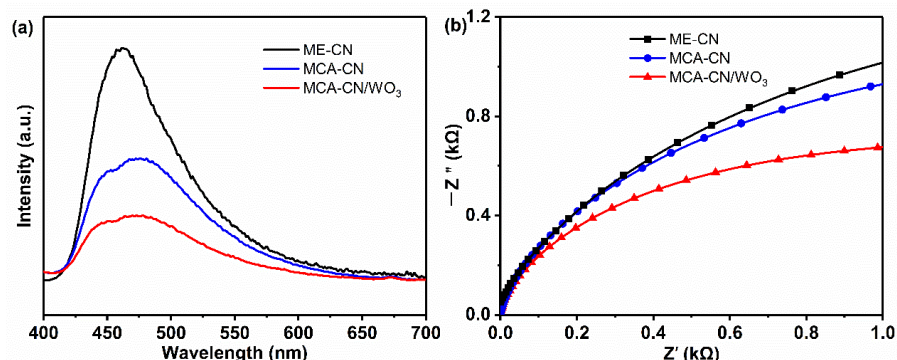


**Figure 7.** (a) PL spectra and (b) EIS Nyquist plots of ME-CN, MCA-CN and MCA-CN/WO<sub>3</sub>.

### 3.3. Catalytic Performance

#### 3.3.1. Photo-Fenton Performance of Catalysts

The catalytic activities of MCA-CN/WO<sub>3</sub> composites were examined by degrading MB in the presence of H<sub>2</sub>O<sub>2</sub> and visible light. As exhibited in Figure 8a, there was little MB degraded in photo-Fenton system without catalysts, indicating the negligible radical production by H<sub>2</sub>O<sub>2</sub> without catalysts. After adding MCA-CN/WO<sub>3</sub> catalysts, the removal

rate of MB reached 98% within 30 min. This result suggested that MCA-CN/WO<sub>3</sub> composites were highly efficient catalysts for H<sub>2</sub>O<sub>2</sub> activation to produce reactive radicals. The MB degradation efficiency of MCA-CN (63%) was higher than that of ME-CN (30%), which ascribed to the larger specific surface area of MCA-CN. MCA-CN/WO<sub>3</sub> exhibited better catalytic performance than MCA-CN, suggesting that the heterojunction between MCA-CN and WO<sub>3</sub> accelerated the decomposition of H<sub>2</sub>O<sub>2</sub> for improving catalytic activity. The MB degradation efficiency of ME-CN/WO<sub>3</sub> (87%) was lower than that of MCA-CN/WO<sub>3</sub>, indicating that the sheet-like structure of MCA-CN can enhance catalytic performance. Moreover, in the MCA-CN/WO<sub>3</sub> photo-Fenton-like process, the degradation rate was higher than when H<sub>2</sub>O<sub>2</sub> (38%) and light (10%) were present alone. This result indicated that the synergistic effect of catalysts, H<sub>2</sub>O<sub>2</sub> and visible light could significantly enhance the removal efficiency of MB. Figure 8b displays the reaction rate constants (*k*) obtained through the Langmuir–Hinshelwood kinetics model. Among all the materials, the rate constant of MCA-CN/WO<sub>3</sub> (0.1465 min<sup>-1</sup>) was the highest, which was about 12.4, 4.7 and 2.1 times higher than that of ME-CN (0.0118 min<sup>-1</sup>), MCA-CN (0.0314 min<sup>-1</sup>) and ME-CN/WO<sub>3</sub> (0.0685 min<sup>-1</sup>). Furthermore, the kinetic constant of MCA-CN/WO<sub>3</sub> in the photo-Fenton-like process was 37.5, 9.5 times higher than its rate constant in the corresponding photocatalytic processes (0.0037 min<sup>-1</sup>) and Fenton-like processes (0.0154 min<sup>-1</sup>). The photo-Fenton degradation of pollutants over g-C<sub>3</sub>N<sub>4</sub>-based photocatalysts is shown in Table S1, and MCA-CN/WO<sub>3</sub> displayed better degradation performance than most of those catalysts.

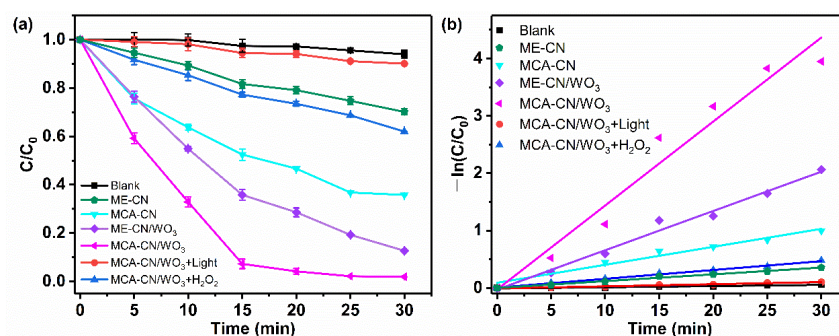


**Figure 8.** (a) Degradation curves of MB under different conditions and (b) reaction rate constants associated with MB degradation.

### 3.3.2. Performance Optimization of MCA-CN/WO<sub>3</sub>

To obtain optimized preparation conditions for high-performance MCA-CN/WO<sub>3</sub>, two experimental parameters were adjusted, the loading amount of WO<sub>3</sub> and the heat treatment temperature. As exhibited in Figure 9a, the removal rate of MB increased gradually as the WO<sub>3</sub> content increased from 5% to 25%. When the content of WO<sub>3</sub> was 35%, there was little improvement in the degradation efficiency. Excess WO<sub>3</sub> induced inter-particle aggregation, thus decreased interfacial contact with MCA-CN and lowered photocatalytic performances. Therefore, the optimal content of WO<sub>3</sub> in the composite was 25%. The degradation properties of catalysts synthesized at temperatures from 300 °C to 450 °C are shown in Figure 9b. Obviously, catalysts synthesized at 300 °C and 350 °C showed better catalytic performance than that at 400 °C and 450 °C. Furthermore, the catalysts synthesized at 300 °C, 350 °C and 450 °C were characterized by XRD (Figure S2). There were no obvious diffraction peaks of WO<sub>3</sub> in the curve of 300 °C MCA-CN/WO<sub>3</sub>, indicating that WO<sub>3</sub> cannot be formed at 300 °C, while there were impure peaks in the curve of 450 °C MCA-CN/WO<sub>3</sub>, owing to the decomposition of MCA-CN. Hence, 350 °C was the most appropriate temperature to synthesize the sample with good catalytic performance.

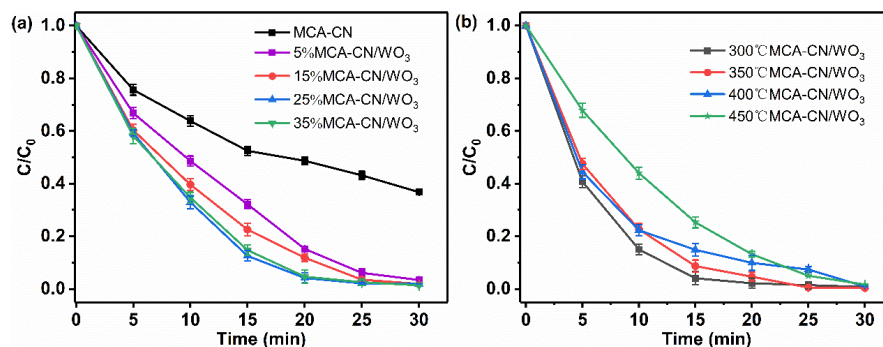


Figure 9. Degradation rate of MB with (a) different loading amount of  $WO_3$  and (b) different synthesized temperatures.

### 3.3.3. The Effect of Experimental Parameters

The effects of pH, amounts of  $H_2O_2$  and catalyst (25% MCA-CN/ $WO_3$ ) on the removal efficiency of MB in the photo-Fenton system were explored to optimize the reaction conditions. It is obvious from Figure 10a that the sample maintained excellent degradation performance in the pH range of 4.3 to 12.3. In addition, the higher the pH value, the better the degradation of MB. About 57% of MB was degraded in 30 min at pH 2.4, but when increasing the pH value to 12.3, the degradation rate reached 99.5% in 30 min. Under acidic conditions, high concentrations of  $H^+$  will scavenge  $HO_2\bullet$  ( $HO_2\bullet + H^+ + e^- \rightarrow H_2O_2$ ) [30], while high pH is beneficial to the survival of  $HO_2\bullet$  and lowers the redox potential of the conduction band to form more  $HO_2\bullet$ . Since  $^1O_2$  formed via  $HO_2\bullet$  was responsible for the removal of MB, there was more  $^1O_2$  produced at a higher pH, improving the MB degradation efficiency.

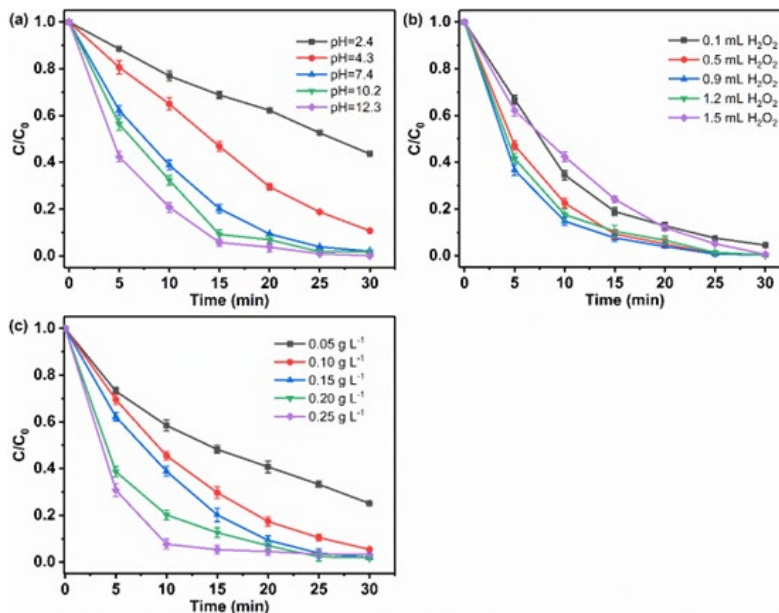


Figure 10. The effect of (a) pH, (b) amount of  $H_2O_2$  and (c) catalyst dosage on degradation of MB in MCA-CN/ $WO_3$ / $H_2O_2$ /visible light system.

$H_2O_2$  is the main substance that generates radicals in the Fenton system. As displayed in Figure 10b, the MB degradation efficiency increased from 95% to 99% in 30 min with an increase in the amount of  $H_2O_2$  from 0.1 to 0.5 mL. The degradation rate of MB improved slightly with the addition of 0.9 mL  $H_2O_2$ . When the amount of  $H_2O_2$  exceeded 0.9 mL, the removal rate decreased with the increase in  $H_2O_2$  content. At high  $H_2O_2$  concentrations, the excess  $H_2O_2$  molecules removed the valuable radical species, resulting in a decrease in

efficiency [31]. Considering both degradation effectiveness and cost, the optimum amount of  $\text{H}_2\text{O}_2$  for the catalytic degradation of MB in the photo-Fenton system was 0.5 mL.

The effect of catalyst amount on the degradation rate is illustrated in Figure 10c. With the catalyst dosage increasing, the degradation rate was faster. However, when the amount of catalyst increased from 0.15 to 0.25  $\text{g L}^{-1}$ , there was almost no difference in the degradation rate at 30 min. Generally, increasing the amount of catalyst would enhance the absorption of light and pollutant, thus improving the catalytic activity. However, from the adsorption curve in Figure S1 (Supplementary Materials), it could be concluded that when the catalyst dosage exceeded 0.20  $\text{g L}^{-1}$ , the removal of pollutants was mainly attributed to adsorption rather than degradation. Hence, in order to study the degradation of MB by catalyst, the optimum amount of the catalyst was 0.15  $\text{g L}^{-1}$ .

### 3.4. Degradation Mechanism

To investigate the mechanism of MB degradation by the MCA-CN/ $\text{WO}_3$  composite, a quenching experiment and EPR analysis were conducted to determine the main active radicals for MB degradation.

In radical quenching tests, IPA, p-BQ, EDTA-2Na and L-His were used to eliminate  $\bullet\text{OH}$ ,  $\bullet\text{O}_2^-$ ,  $\text{h}^+$  and  $^1\text{O}_2$ , respectively. As exhibited in Figure 11a, the degradation rate of MB decreased slightly when IPA, EDTA-2Na and p-BQ were added into the system. However, the degradation of MB decreased from 98% to 40% within 30 min after the adding of L-His. The results indicated that  $^1\text{O}_2$  radicals were responsible for MB removal in the photo-Fenton system of the MCA-CN/ $\text{WO}_3$  composite, while  $\bullet\text{OH}$ ,  $\bullet\text{O}_2^-$  and  $\text{h}^+$  had a slight effect on MB degradation.

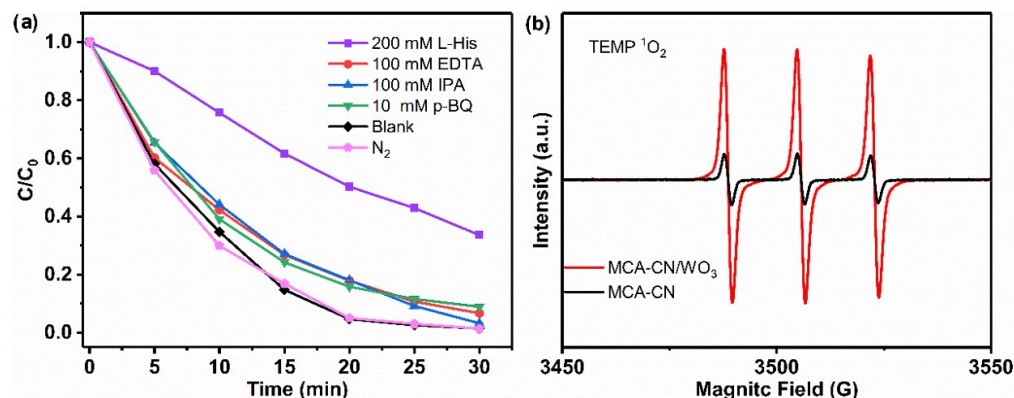
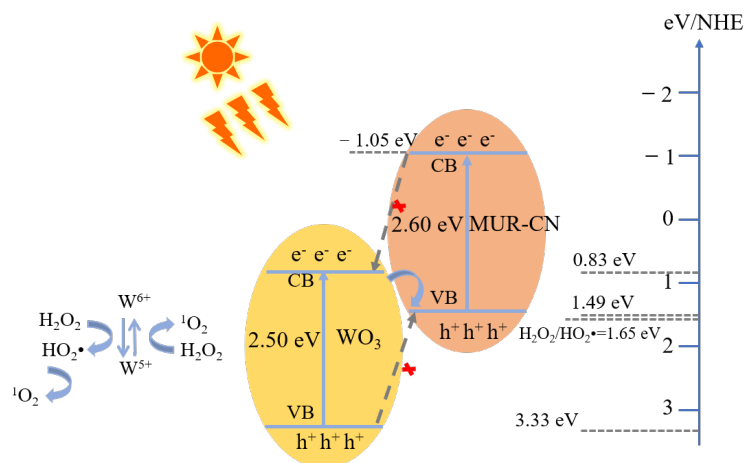


**Figure 11.** (a) Quenching experiment of different radicals and (b) EPR spectra for TEMP adducts in photo-Fenton-like system of MCA-CN and MCA-CN/ $\text{WO}_3$ .

EPR analysis was conducted to confirm the role of  $^1\text{O}_2$  in the reaction. The  $^1\text{O}_2$  was captured by TEMP and generated a 1:1:1 triplet signal, as displayed in Figure 11b. In comparison with bare MCA-CN system, the signal produced in the MCA-CN/ $\text{WO}_3$  system was much stronger, indicating that more  $^1\text{O}_2$  was produced in the MCA-CN/ $\text{WO}_3$  system. This was consistent with the previous results shown in Figure 11a, demonstrating that  $^1\text{O}_2$  played a critical role for the removal of MB. Typically,  $^1\text{O}_2$  can be generated through three pathways: (1) the oxidation of  $\bullet\text{O}_2^-$  produced by  $\text{O}_2$  [32]; (2) The Haber–Weiss reaction between  $\bullet\text{O}_2^-/\text{HO}_2\bullet$  and  $\text{H}_2\text{O}_2$  [33]; (3) the recombination of  $\bullet\text{O}_2^-/\text{HO}_2\bullet$  [34]. To explore the origin of  $^1\text{O}_2$ , the degradation rate of MB with MCA-CN/ $\text{WO}_3$  in nitrogen atmosphere was tested. As depicted in Figure 11a, the MB degradation remained unchanged in the presence of  $\text{N}_2$ , indicating that  $\text{O}_2$  was not the precursor of  $^1\text{O}_2$  in this reaction. Therefore, we could speculate that  $\text{H}_2\text{O}_2$  was the only source for  $^1\text{O}_2$  generation in the MCA-CN/ $\text{WO}_3$  photo-Fenton system. As displayed in radical quenching tests,  $\bullet\text{O}_2^-$  had little effect on MB degradation. Hence, it was speculated that  $\text{H}_2\text{O}_2$  was converted into  $^1\text{O}_2$  via the Haber–Weiss reaction between  $\text{HO}_2\bullet$  and  $\text{H}_2\text{O}_2$ , or the recombination of  $\text{HO}_2\bullet$ . The

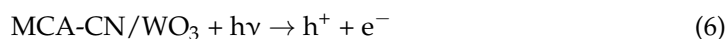
reaction rate constant of  $\text{HO}_2\bullet$  recombination is  $8.3 \times 10^5 \text{ M}^{-1} \text{ s}^{-1}$  [35], which is about five magnitudes larger than that of  $\text{HO}_2\bullet$  and  $\text{H}_2\text{O}_2$  ( $3 \text{ M}^{-1} \text{ s}^{-1}$ ) [36,37]. Therefore,  $\text{HO}_2\bullet$  recombination was dominant for  $^1\text{O}_2$  generation in the photo-Fenton system of the MCA-CN/ $\text{WO}_3$  catalyst.

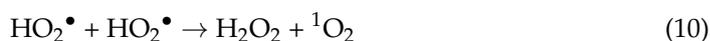
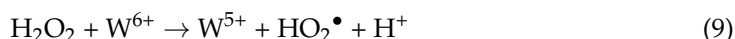
The energy band structures of MCA-CN/ $\text{WO}_3$  obtained by UV-Vis DRS are shown in Figure 12. For such an energy band structure, there are usually two possible charge transfer mechanisms: (1) type II heterojunctions and (2) Z-scheme heterojunctions [38]. Supposing there is a type II heterojunction between MCA-CN and  $\text{WO}_3$ , photogenerated holes are transferred from the VB of  $\text{WO}_3$  to the VB of MCA-CN, while photogenerated electrons are transferred from the CB of MCA-CN to the CB of  $\text{WO}_3$  with a positive potential (grey dashed line in Figure 12). However, due to the lower reduction potential of  $\text{H}_2\text{O}_2/\text{HO}_2\bullet$  ( $E^0 = 1.65 \text{ V. NHE}$ ) than the VB potentials of MCA-CN (1.49 eV) [39], the holes on the VB of MCA-CN cannot decompose  $\text{H}_2\text{O}_2$  into  $\text{HO}_2\bullet$ . This is not consistent with the above conclusion that  $^1\text{O}_2$  is produced by  $\text{HO}_2\bullet$ . For a Z-scheme heterojunction, the electrons on the CB of  $\text{WO}_3$  are transferred to the VB of MCA-CN (solid blue line in Figure 12), and the VB potential of  $\text{WO}_3$  (3.12 eV) is lower than  $\text{H}_2\text{O}_2/\text{HO}_2\bullet$  ( $E^0 = 1.65 \text{ V. NHE}$ ), allowing the production of  $\text{HO}_2\bullet$ . The above analysis suggested that the charge transfer mechanism of MCA-CN/ $\text{WO}_3$  was Z-scheme.



**Figure 12.** Schematic illustration of catalytic mechanism of MCA-CN/ $\text{WO}_3$  in photo-Fenton-like process.

A possible photo-Fenton-like catalytic mechanism for MB degradation on the MCA-CN/ $\text{WO}_3$  composite was proposed, as illustrated in Figure 12 and the following equations. Under visible light irradiation, both  $\text{WO}_3$  and MCA-CN were activated, along with the generation of electron-hole pairs. Electrons from the CB of  $\text{WO}_3$  transferred spontaneously to the VB of MCA-CN to recombine with the holes from MCA-CN. Accordingly, most of the electrons were accumulated on the CB of MCA-CN, while the predominated holes were inhabited on the VB of  $\text{WO}_3$ . In this way, holes and electrons were separated effectively (Equation (6)), which attributed to the Z-scheme heterojunction between  $\text{WO}_3$  and MCA-CN nanosheets. In the traditional Fenton system, radicals can be generated through the decomposition of  $\text{H}_2\text{O}_2$  catalyzed by  $\text{Fe}^{2+}/\text{Fe}^{3+}$  [40]. Similarly, the conversion between  $\text{W}^{6+}$  and  $\text{W}^{5+}$  could promote the decomposition of  $\text{H}_2\text{O}_2$  [16].  $\text{W}^{6+}$  gained an electron to form  $\text{W}^{5+}$ , and  $\text{W}^{5+}$  decomposed  $\text{H}_2\text{O}_2$  into  $^1\text{O}_2$  by the oxidation of  $\text{h}^+$  (Equations (7) and (8)). In addition,  $\text{HO}_2\bullet$  was produced by the reaction between  $\text{H}_2\text{O}_2$  and  $\text{W}^{6+}$  (Equation (9)), subsequently recombined to form  $^1\text{O}_2$  (Equation (10)). Ultimately, the plentiful active species  $^1\text{O}_2$  decomposed MB into  $\text{CO}_2$ ,  $\text{H}_2\text{O}$  and degradation intermediates (Equation (11)) [41,42].





To investigate the degradation pathways of MB in the photo-Fenton-like process, the intermediate products at 30 min of the reaction were determined using LC-MS. The structures of the intermediates were obtained through the Nist standard database and are listed in Table S2 (Supplementary Materials) and Figure S3 (Supplementary Materials), showing the mass spectrum of intermediates. Degradation pathways are shown in Figure 13. Among the molecules of MB, the C-S molecular bond has the smallest bond energy and is easy to break. The N of the C-N bond is also susceptible to be oxidated because of its low electronegativity. Under the attack of  ${}^1\text{O}_2$ , the bond between the methyl group and C was cracked. In pathway 1, the MB was changed into intermediate A when S was oxidized to S=O. The intermediate A was transformed to intermediate B when the C-N bonds broke. Then, the C-S bond broke and intermediate B was transformed to intermediate C. In pathway 2, the MB was changed into intermediate D owing to the cracking of C-S bonds. With the strong oxidation capacity of  ${}^1\text{O}_2$  and  $\bullet\text{OH}$ , intermediate D is oxidized to form intermediate E. As the reaction continued, intermediate C and intermediate E would decompose into small molecule organic acids,  $\text{SO}_4^{2-}$ ,  $\text{NO}_3^-$ ,  $\text{CO}_2$  and  $\text{H}_2\text{O}$ .

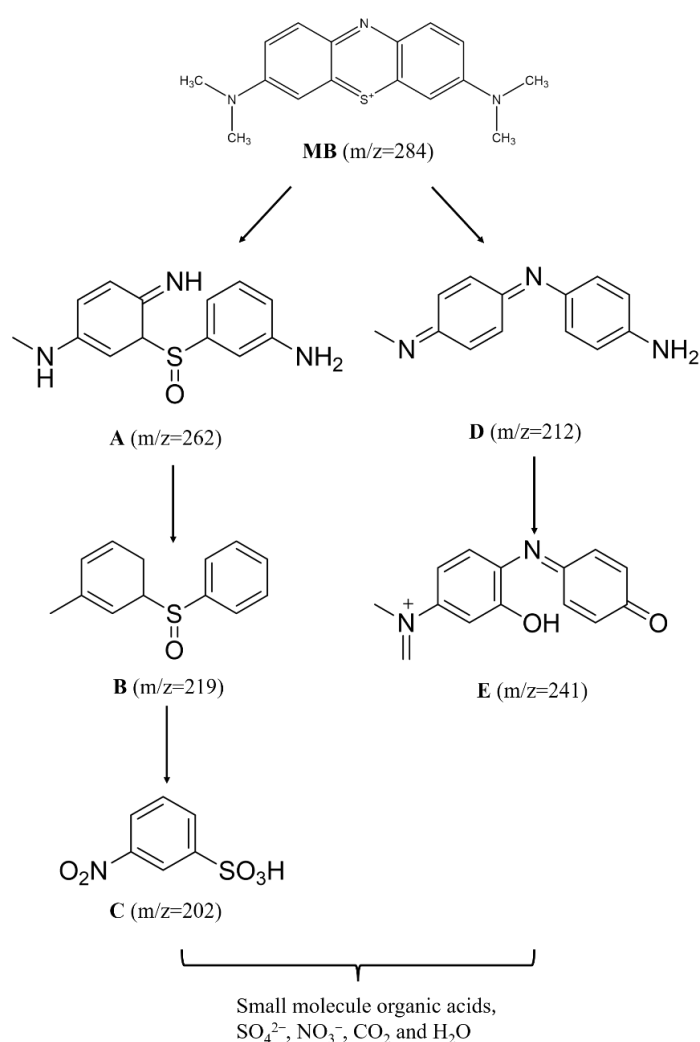


**Figure 13.** Possible pathways of MB degradation in MCA-CN/ $\text{WO}_3$ / $\text{H}_2\text{O}_2$ /visible light system.

### 3.5. Stability of MCA-CN/WO<sub>3</sub> Catalyst

The stability of a catalyst is one of the most important indexes of its practicability. A cycling experiment was conducted to evaluate the reusability of MCA-CN/WO<sub>3</sub>. As shown in Figure 14a, even after five cycles, the MCA-CN/WO<sub>3</sub> catalyst exhibited high catalytic performance, degrading 85% of the MB in 30 min. The XRD spectra of the five cycles of MCA-CN/WO<sub>3</sub> used were carried out (Figure 14b). Compared with the XRD patterns of the fresh MCA-CN/WO<sub>3</sub> catalyst, the diffraction peak of MCA-CN/WO<sub>3</sub> after five cycles did not change greatly, indicating the good stability and reusability of the MCA-CN/WO<sub>3</sub> catalyst.

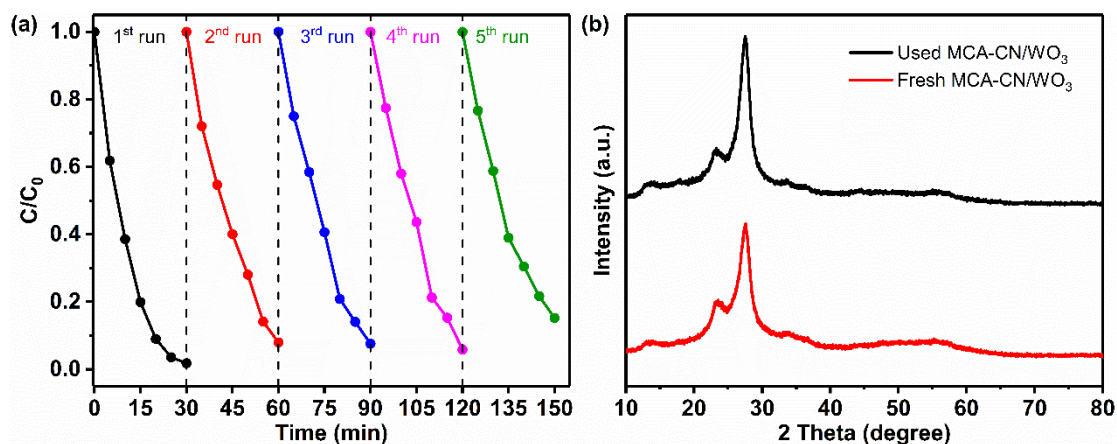


**Figure 14.** (a) Recycling tests of MCA-CN/WO<sub>3</sub> in MB degradation and (b) XRD patterns of fresh MCA-CN/WO<sub>3</sub> and used MCA-CN/WO<sub>3</sub>.

## 4. Conclusions

In this study, MCA-CN/WO<sub>3</sub> catalysts were prepared by thermal treatment for MB degradation in photo-Fenton-like processes. The removal efficiency of MB using MCA-CN/WO<sub>3</sub> reached 98% in 30 min, of which the rate constant was about 12.4, 4.7 and 2.1 times higher than that of ME-CN, MCA-CN and ME-CN/WO<sub>3</sub>. Such enhanced catalytic performance was mainly attributed to the Z-scheme heterojunction between MCA-CN and WO<sub>3</sub>, which accelerated the charge transfer and inhibited the recombination of electrons and holes. In addition, the nanosheet structure and large specific surface area shortened the charge transfer distance and provided abundant active sites, thus improving the catalytic performance of MCA-CN/WO<sub>3</sub>. The introduction of WO<sub>3</sub> enhanced the visible light absorption capacity and further promoted the separation of electron–hole pairs. All of these advantages facilitated the decomposition of H<sub>2</sub>O<sub>2</sub> to produce <sup>1</sup>O<sub>2</sub> for the degradation of MB. This study provided a reference to prepare a WO<sub>3</sub>-loaded porous carbon nitride nanosheet catalyst for MB degradation in the photo-Fenton-like process.

**Supplementary Materials:** The following are available online at <https://www.mdpi.com/article/10.3390/w14162569/s1>, Figure. S1 Removal rate of MB by absorption. Figure. S2 XRD patterns of MCA-CN/WO<sub>3</sub>, 300 °C MCA-CN/WO<sub>3</sub> and 450 °C MCA-CN/WO<sub>3</sub>. Figure. S3 Different retention time of LC-MS spectrum: (a) 5.75min, (b) 5.13 min, (c) 4.96min, (d) 2.77 min and (e) 2.45 min. Table S1 Summary of the photo-Fenton degradation of pollutants over g-C<sub>3</sub>N<sub>4</sub>-based photocatalysts. Table S2 Retention time, mass spectra and chemical structure of main degradation intermediates of MB. For more details, please see [5,20,43–46].

**Author Contributions:** Conceptualization, W.G. and X.Z.; methodology, W.G. and X.Z.; software, W.G.; validation, W.G.; formal analysis, W.G., G.Z., X.Z., S.Z. and Z.W.; investigation, W.G.; resources, W.G.; data curation, W.G.; writing—original draft preparation, W.G.; writing—review and editing, W.G. and X.Z.; visualization, W.G.; supervision, W.G. and X.Z.; project administration, X.Z. and S.Z.; funding acquisition, X.Z. All authors have read and agreed to the published version of the manuscript.

**Funding:** This research was funded by the National Key Research and Development Program of China (Grant No. 2016YFC0400702-2), the National Natural Science Foundation of China (Grant No. 21377041), the Guangdong Science and Technology Program (2020B121201003).

**Institutional Review Board Statement:** Not applicable.

**Informed Consent Statement:** Not applicable.

**Data Availability Statement:** Not applicable.

**Conflicts of Interest:** The funders had no role in the design of the study; in the collection, analyses, or interpretation of data; in the writing of the manuscript, or in the decision to publish the results.

## References

1. Li, X.N.; Ao, Z.M.; Liu, J.Y.; Sun, H.Q.; Rykov, A.I.; Wang, J.H. Topotactic transformation of metal–organic frameworks to graphene-encapsulated transition-metal nitrides as efficient Fenton-like catalysts. *ACS Nano* **2016**, *10*, 11532–11540. [[CrossRef](#)]
2. Wols, B.A.; Hofman-Caris, C.H. Review of photochemical reaction constants of organic micropollutants required for UV advanced oxidation processes in water. *Water Res.* **2012**, *46*, 2815–2827. [[CrossRef](#)]
3. Zhu, J.N.; Zhu, X.Q.; Cheng, F.F.; Li, P.; Wang, F.; Xiao, Y.W.; Xiong, W.W. Preparing copper doped carbon nitride from melamine templated crystalline copper chloride for Fenton-like catalysis. *Appl. Catal. B Environ.* **2019**, *256*, 117830. [[CrossRef](#)]
4. Lim, H.; Lee, J.; Jin, S.; Kim, J.; Yoon, J.; Hyeon, T. Highly active heterogeneous Fenton catalyst using iron oxide nanoparticles immobilized in alumina coated mesoporous silica. *Chem. Commun.* **2006**, *4*, 463–465. [[CrossRef](#)]
5. Ma, Y.L.; Zhang, J.; Wang, Y.; Chen, Q.; Feng, Z.M.; Sun, T. Concerted catalytic and photocatalytic degradation of organic pollutants over CuS/g-C<sub>3</sub>N<sub>4</sub> catalysts under light and dark conditions. *J. Adv. Res.* **2019**, *16*, 135–143. [[CrossRef](#)]
6. Hu, P.D.; Long, M. Cobalt-catalyzed sulfate radical-based advanced oxidation: A review on heterogeneous catalysts and applications. *Appl. Catal. B Environ.* **2016**, *181*, 103–117. [[CrossRef](#)]
7. Barrio, J.; Lin, L.; Amo-Ochoa, P.; Tzadikov, J.; Peng, G.; Sun, J.; Shalom, M. Unprecedented centimeter-long carbon nitride needles: Synthesis, characterization and applications. *Small* **2018**, *14*, e1800633. [[CrossRef](#)]
8. Sun, S.D.; Liang, S.H. Recent advances in functional mesoporous graphitic carbon nitride (mpg-C<sub>3</sub>N<sub>4</sub>) polymers. *Nanoscale* **2017**, *9*, 10544–10578. [[CrossRef](#)]
9. Xu, R.P.; Li, J.; Sui, G.Z.; Zhuang, Y.; Guo, D.X.; Luo, Z.; Chen, S. Constructing supramolecular self-assembled porous g-C<sub>3</sub>N<sub>4</sub> nanosheets containing thiophene-groups for excellent photocatalytic performance under visible light. *Appl. Surf. Sci.* **2022**, *578*, 152064. [[CrossRef](#)]
10. Fattahimoghaddam, H.; Mahvelati-Shamsabadi, T.; Lee, B.K. Efficient photodegradation of Rhodamine B and tetracycline over robust and green g-C<sub>3</sub>N<sub>4</sub> nanostructures supramolecular design. *J. Hazard. Mater.* **2021**, *403*, 123703. [[CrossRef](#)]
11. Zhang, K.; Jin, Y.R.; Guo, Y.X.; Wang, H.W.; Liu, K.F.; Fu, W.J.; Wang, B. Study on Microstructure and Photocatalytic Mechanism of g-C<sub>3</sub>N<sub>4</sub>/WO<sub>3</sub> Heterojunctions Prepared by Ice Template. *Chem. Sel.* **2021**, *6*, 5719–5728. [[CrossRef](#)]
12. Meng, J.Q.; Wang, X.Y.; Liu, Y.Q.; Ren, M.; Zhang, X.Y.; Ding, X.H.; Yang, Y. Acid-induced molecule self-assembly synthesis of Z-scheme WO<sub>3</sub>/g-C<sub>3</sub>N<sub>4</sub> heterojunctions for robust photocatalysis against phenolic pollutants. *Chem. Eng. J.* **2021**, *403*, 126354. [[CrossRef](#)]
13. Li, X.; Song, X.H.; Ma, C.C.; Cheng, Y.M.; Shen, D.; Zhang, S.M.; Wang, H. Direct Z-Scheme WO<sub>3</sub>/graphitic carbon nitride nanocomposites for the photoreduction of CO<sub>2</sub>. *ACS Appl. Nano Mater.* **2020**, *3*, 1298–1306.
14. Jun, Y.S.; Lee, E.Z.; Wang, X.; Hong, W.H.; Stucky, G.D.; Thomas, A. From Melamine-Cyanuric acid supramolecular aggregates to carbon nitride hollow spheres. *Adv. Funct. Mater.* **2013**, *23*, 3661–3667. [[CrossRef](#)]
15. Song, T.; Xie, C.; Matras-Postolek, K.; Yang, P. 2D layered g-C<sub>3</sub>N<sub>4</sub>/WO<sub>3</sub>/WS<sub>2</sub> S-Scheme heterojunctions with enhanced photochemical performance. *J. Chem. A* **2021**, *125*, 19382–19393. [[CrossRef](#)]
16. Bai, X.Y.; Li, Y.; Xie, L.B.; Liu, X.H.; Zhan, S.H.; Hu, W.P. A novel Fe-free photo-electro-Fenton-like system for enhanced ciprofloxacin degradation: Bifunctional Z-scheme WO<sub>3</sub>/g-C<sub>3</sub>N<sub>4</sub>. *Environ. Sci. Nano* **2019**, *6*, 2850–2862. [[CrossRef](#)]
17. Singh, J.; Arora, A.; Basu, S. Synthesis of coral like WO<sub>3</sub>/g-C<sub>3</sub>N<sub>4</sub> nanocomposites for the removal of hazardous dyes under visible light. *J. Alloys Compd.* **2019**, *808*, 151734. [[CrossRef](#)]
18. Wang, X.; Maeda, K.; Thomas, A.; Takanabe, K.; Xin, G.; Carlsson, J.M.; Antonietti, M. A metal-free polymeric photocatalyst for hydrogen production from water under visible light. *Nat. Mater.* **2009**, *8*, 76–80. [[CrossRef](#)]
19. Yang, S.B.; Gong, Y.J.; Zhang, J.L.; Zhan, L.; Ma, L.S.; Fang, Z.Y.; Ajayan, P.M. Exfoliated graphitic carbon nitride nanosheets as efficient catalysts for hydrogen evolution under visible light. *Adv. Mater.* **2013**, *25*, 2452–2456. [[CrossRef](#)]
20. Xi, J.H.; Xia, H.; Ning, X.M.; Zhang, Z.; Liu, J.; Mu, Z.J.; Lu, X. Carbon-Intercalated 0D/2D hybrid of hematite quantum dots/graphitic carbon nitride nanosheets as superior catalyst for advanced oxidation. *Small* **2019**, *15*, e1902744. [[CrossRef](#)]
21. Liang, Q.H.; Li, Z.; Yu, X.L.; Huang, Z.H.; Kang, F.Y.; Yang, Q.H. Macroscopic 3D porous graphitic carbon nitride monolith for enhanced photocatalytic hydrogen evolution. *Adv. Mater.* **2015**, *27*, 4634–4639. [[CrossRef](#)]
22. Zhu, W.Y.; Sun, F.Q.; Goei, R.; Zhou, Y. Construction of WO<sub>3</sub>-g-C<sub>3</sub>N<sub>4</sub> composites as efficient photocatalysts for pharmaceutical degradation under visible light. *Catal. Sci. Technol.* **2017**, *7*, 2591–2600. [[CrossRef](#)]

23. Ding, J.; Liu, Q.Q.; Zhang, Z.Y.; Liu, X.; Zhao, J.Q.; Cheng, S.B.; Dai, W.L. Carbon nitride nanosheets decorated with WO<sub>3</sub> nanorods: Ultrasonic-assisted facile synthesis and catalytic application in the green manufacture of dialdehydes. *Appl. Catal. B Environ.* **2015**, *165*, 511–518. [[CrossRef](#)]
24. Song, T.; Zhang, X.; Yang, P. Bifunctional nitrogen-doped carbon dots in g-C<sub>3</sub>N<sub>4</sub>/WO<sub>x</sub> heterojunction for enhanced photocatalytic water-splitting performance. *Langmuir* **2021**, *37*, 4236–4247. [[CrossRef](#)]
25. Zeng, Y.X.; Liu, C.B.; Wang, L.L.; Zhang, S.Q.; Ding, Y.B.; Xu, Y.Z.; Luo, S. A three-dimensional graphitic carbon nitride belt network for enhanced visible light photocatalytic hydrogen evolution. *J. Mater. Chem.* **2016**, *4*, 19003–19010. [[CrossRef](#)]
26. Liu, D.; Zhang, S.A.; Wang, J.M.; Peng, T.; Li, R.J. Direct Z-Scheme 2D/2D photocatalyst based on ultrathin g-C<sub>3</sub>N<sub>4</sub> and WO<sub>3</sub> nanosheets for efficient visible-light-driven H<sub>2</sub> generation. *ACS Appl. Mater. Interfaces* **2019**, *11*, 27913–27923. [[CrossRef](#)]
27. Li, X.; Kang, B.B.; Dong, F.; Zhang, Z.Q.; Luo, X.D.; Han, L.; Wang, Z.L. Enhanced photocatalytic degradation and H<sub>2</sub>/H<sub>2</sub>O<sub>2</sub> production performance of S-pCN/WO<sub>2.72</sub> S-scheme heterojunction with appropriate surface oxygen vacancies. *Nano Energy* **2021**, *81*, 105671. [[CrossRef](#)]
28. Wang, J.J.; Wang, Z.Y.; Liu, C.J.J. Enhanced activity for CO oxidation over WO<sub>3</sub> nanolamella supported Pt catalyst. *ACS Appl. Mater. Interfaces* **2014**, *6*, 12860–12867. [[CrossRef](#)]
29. Chen, X.K.; Li, H.; Wu, Y.S.; Wu, H.; Wu, L.F.; Tan, P.; Xiong, X. Facile fabrication of novel porous graphitic carbon nitride/copper sulfide nanocomposites with enhanced visible light driven photocatalytic performance. *J. Colloid. Interf. Sci.* **2016**, *476*, 132–143. [[CrossRef](#)]
30. Ahmed, Y.; Yaakob, Z.; Akhtar, P. Degradation and mineralization of methylene blue using a heterogeneous photo-Fenton catalyst under visible and solar light irradiation. *Catal. Sci. Technol.* **2016**, *6*, 1222–1232. [[CrossRef](#)]
31. Muruganandham, M.; Swaminathan, M. Photocatalytic decolourisation and degradation of Reactive Orange 4 by TiO-UV process. *Dye. Pigment.* **2006**, *68*, 133–142. [[CrossRef](#)]
32. Yi, Q.Y.; Ji, J.; Shen, B.; Dong, C.C.; Liu, J.; Zhang, J.L.; Xing, M. Singlet oxygen triggered by superoxide radicals in a molybdenum cocatalytic Fenton reaction with enhanced redox activity in the environment. *Environ. Sci. Technol.* **2019**, *53*, 9725–9733. [[CrossRef](#)]
33. Zhao, Y.M.; Sun, M.; Wang, X.X.; Wang, C.; Lu, D.W.; Ma, W.; Elimelech, M. Janus electrocatalytic flow-through membrane enables highly selective singlet oxygen production. *Nat. Commun.* **2020**, *11*, 6228. [[CrossRef](#)]
34. Yang, Z.C.; Qian, J.S.; Yu, A.Q.; Pan, B.C. Singlet oxygen mediated iron-based Fenton-like catalysis under nanoconfinement. *Proc. Natl. Acad. Sci. USA* **2019**, *116*, 6659–6664. [[CrossRef](#)]
35. Pignatello, J.J.; Oliveros, E.; MacKay, A. Advanced oxidation processes for organic contaminant destruction based on the fenton reaction and related chemistry. *Crit. Rev. Environ. Sci. Technol.* **2006**, *36*, 1–84. [[CrossRef](#)]
36. Laura, A.; MacManus-Spencer, K.M. Quantification of singlet oxygen production in the reaction of superoxide with hydrogen peroxide using a selective chemiluminescent. *Probe* **2005**, *127*, 8954–8955. [[CrossRef](#)]
37. Zheng, N.C.; He, X.; Hu, R.T.; Wang, R.L.; Zhou, Q.; Lian, Y.K.; Hu, Z. In-situ production of singlet oxygen by dioxygen activation on iron phosphide for advanced oxidation processes. *Appl. Catal. B Environ.* **2022**, *307*, 121157. [[CrossRef](#)]
38. Jia, J.K.; Jiang, C.Y.; Zhang, X.R.; Li, P.J.; Xiong, J.X.; Zhang, Z.Z.; Wang, Y. Urea-modified carbon quantum dots as electron mediator decorated g-C<sub>3</sub>N<sub>4</sub>/WO<sub>3</sub> with enhanced visible-light photocatalytic activity and mechanism insight. *Appl. Surf. Sci.* **2019**, *495*, 143524. [[CrossRef](#)]
39. Jain, B.; Singh, A.K.; Kim, H.; Lichtfouse, E.; Sharma, V.K. Treatment of organic pollutants by homogeneous and heterogeneous Fenton reaction processes. *Environ. Chem. Lett.* **2018**, *16*, 947–967. [[CrossRef](#)]
40. Zhao, H.Y.; Chen, Y.; Peng, Q.S.; Wang, Q.N.; Zhao, G.H. Catalytic activity of MOF(2Fe/Co)/carbon aerogel for improving H<sub>2</sub>O<sub>2</sub> and OH generation in solar photo-electro-Fenton process. *Appl. Catal. B Environ.* **2017**, *203*, 127–137. [[CrossRef](#)]
41. Yin, Y.; Ren, Y.; Lu, J.H.; Zhang, W.M.; Shan, C.; Hua, M.; Pan, B. The nature and catalytic reactivity of UiO-66 supported Fe<sub>3</sub>O<sub>4</sub> nanoparticles provide new insights into Fe-Zr dual active centers in Fenton-like reactions. *Appl. Catal. B Environ.* **2021**, *286*, 119943. [[CrossRef](#)]
42. Zhou, S.Q.; Wang, Y.; Zhou, K.; Ba, D.Y.; Ao, Y.H.; Wang, P.F. In-situ construction of Z-scheme g-C<sub>3</sub>N<sub>4</sub>/WO<sub>3</sub> composite with enhanced visible-light responsive performance for nitenpyram degradation. *Chin. Chem. Lett.* **2021**, *32*, 2179–2182. [[CrossRef](#)]
43. Wang, L.; Zhu, Y.; Yang, D.; Zhao, L.; Ding, H.; Wang, Z. The mixed marriage of copper and carbon ring-g-C<sub>3</sub>N<sub>4</sub> nanosheet: A visible-light-driven heterogeneous Fenton-like catalyst. *Appl. Surf. Sci.* **2019**, *488*, 728–738. [[CrossRef](#)]
44. Zhang, J.; Zhang, G.; Ji, Q.H.; Lan, H.C.; Qu, J.H.; Liu, H.J. Carbon nanodot-modified FeOCl for photo-assisted Fenton reaction featuring synergistic in-situ H<sub>2</sub>O<sub>2</sub> production and activation. *Appl. Catal. B* **2020**, *266*, 118665. [[CrossRef](#)]
45. An, S.F.; Zhang, G.H.; Wang, T.W.; Zhang, W.N.; Li, K.; Song, C.S. nHigh-Density Ultra-small Clusters and Single-Atom Fe Sites Embedded in Graphitic Carbon Nitride (g-C<sub>3</sub>N<sub>4</sub>) for Highly Efficient Catalytic Advanced Oxidation Processes. *ACS Nano* **2018**, *12*, 9441–9450. [[CrossRef](#)]
46. Li, X.; Pi, Y.H.; Wu, L.Q.; Xia, Q.B.; Wu, J.L.; Li, Z. Facilitation of the visible light-induced Fenton-like excitation of H<sub>2</sub>O<sub>2</sub> via heterojunction of g-C<sub>3</sub>N<sub>4</sub>/NH<sub>2</sub>-Iron terephthalate metal-organic framework for MB degradation. *Appl. Catal. B* **2017**, *202*, 653–663. [[CrossRef](#)]